Interfacial Photopolymerization: A Method for Light-Based Printing of Thermoplastics

Cécile A. C. Chazot,*,†,‡,§ Megan A. Creighton,*,¶,‡ and A. John Hart*,‡

†Department of Materials Science and Engineering, Massachusetts Institute of Technology,
77 Massachusetts Avenue, Cambridge, Massachusetts 02139, United States

‡Department of Mechanical Engineering, Massachusetts Institute of Technology, 77

Massachusetts Avenue, Cambridge, Massachusetts 02139, United States

¶Department of Chemical and Biological Engineering, Drexel University, 3141 Chestnut

Street, Philadelphia, PA 19104, United States

§Current address: Department of Materials Science and Engineering Northwestern
University, 2220 Campus Drive, Evanston, IL 60208-3108, USA

E-mail: cchazot@mit.edu; mc4298@drexel.edu; ajhart@mit.edu

Abstract

Ultraviolet printing of photopolymers is a widely adopted polymer manufacturing method because of its superior resolution and high throughput. However, the available printable photopolymer are typically thermosets, resulting in challenges in post-processing and recycling of the printed structures. Here, we present a new process called interfacial photopolymerization (IPP) which enables photopolymerization printing of linear chain polymers. In IPP, a polymer film is formed at the interface between two immiscible liquids, one containing a chain-growth monomer and the other containing a photoinitiator. We demonstrate the integration of IPP in a proof-of-concept projection system printing polyacrylonitrile (PAN). This is the first report of photopolymerization printing of PAN, a high-performance linear chain polymer. IPP shows in-plane

and out-of-plane resolutions comparable to conventional photoprinting methods. Cohesive PAN films with number average molecular weight greater than 15kg mol⁻¹ are obtained. A macrokinetics model of IPP is provided to deepen understanding of the transport and reaction rates involved and evaluate how reaction parameters affect film thickness and print speed. Last, demonstration of IPP in a multilayer scheme suggests the suitability of the method for multidimensional printing of linear-chain polymers.

Introduction

Methods for scalable manufacturing of polymeric materials with tailored geometries and surface topographies have been instrumental to many industries and applications, including filtration/separation, ¹ microelectronics, ² photonics, ³ biotechnology, ^{4,5} and tissue engineering, ^{6,7} In this regard, many photocurable polymers are used in high-throughput manufacturing of thin films with micro- and nanoscale topography and patterning, engineered coatings, and digital graphics printing. These methods include 2D micro- and nanoscale processes such as photolithography, ⁸ UV inkjet printing, ^{9,10} and the formation of three-dimensional objects through vat polymerization additive manufacturing (or 3D printing). ^{11–13}

Printing of photopolymers relies on cross-linking of polymer chains and macromolecular network formation to solidify the polymer and establish thermal and chemical stability. ^{14,15} The thermoset nature of the printed structures results in challenges in both their post-processing and recycling,. ¹⁶ While researchers have proposed alternative thermoset polymer systems such as covalent adaptable networks (CANs) ¹⁷ or thermosets based on biodegradable linear chain polymers, ^{16,18} none of these solutions provide the quality and mechanical properties of state-of-the-art photopolymerized products. ¹⁶

In contrast, thermoplastic processing methods such as injection molding, ¹⁹ thermoforming, ²⁰ or fused filament fabrication (FFF) 3D printing ²¹ have broader appeal. This is due to the thermoplastics' processability and recyclability combined with the range of accessible mechanical and thermal properties offered by the variety of available linear chain polymers.

However, patterning of thermoplastics at fine length scales is limited by their high melt viscosity; for instance, the smallest features achievable in thermoforming and injection molding are limited both by fabrication of forming tools and by the high capillary forces and rapid cooling rates from the large surface-to-volume ratio and contact area with the forming tool. ²² This can be accompanied by anisotropic properties compared to the bulk material due to undesirable polymer crystallization or shear-induced alignment. ²³

A method for high-resolution, high-throughput photoprinting of linear chain polymers would enable both on-demand production of high-resolution objects with attractive mechanical properties and potential recyclability. Herein, we describe a novel UV photoprinting method to achieve this goal, called interfacial photopolymerization (IPP). IPP relies on controlled free-radical photopolymerization at an immiscible liquid-liquid interface. This mechanism contrasts well-established photoprinting methods such as vat polymerization 3D printing or inkjet UV printing, which involve a single phase resin and precipitation of a solid objects by chemical crosslinking. We elucidate the process requirements based on the transport and reaction kinetics of non-photoinitiated interfacial polymerization (IP) reactions, ²⁴ and demonstrate the technique on poly(acrylonitrile) (PAN), as a model linear-chain and recyclable ^{25–28} polymer system. Through a single-layer printing process, we assess the inplane and out-of-plane resolution of the IPP printing process and how it depends on process parameters such as photoinitiator type and concentration. We also derive a first-principle macrokinetics model of the diffusion, free-radical polymerization reaction, and precipitation at the interface to establish quantitative understanding of how single layers form in IPP. Last, we demonstrate that IPP can be implemented in a multilayer scheme, showing future potential for light-based 3D printing of other linear chain polymers.

Results and Discussion

Key considerations for IPP

In contrast to existing photopolymerization printing methods that rely on bulk polymerization from a single resin phase, IPP relies on a reactive interface between two immiscible liquids. In IPP, the photoinitiator and the monomer are segregated between the two liquids, such that photoinitiated free-radical polymerization can only occur near the liquid-liquid interface (Figure 1a). Here, we considered the reaction of a water-soluble photoinitiator with a water-immiscible liquid monomer as the organic phase. Full details of the materials, experimental methods, and characterization techniques are provided in the Supporting Information.

In addition to the formation of a stable liquid-liquid interface, the IPP system must satisfy two main requirements to enable the polymer film to form and retain its geometry in absence of crosslinking. First, the monomeric organic phase must be sparingly soluble in water, such that both the monomer and initiator are present in a shallow region near the liquid-liquid interface which we call the reaction zone (Figure 1b). Upon UV light exposure of the interface, the initiator is dissociated, generating free radicals that react and consume local monomer in a polyaddition reaction scheme. Second, the resulting polymer must be insoluble in both phases to successfully precipitate (Figure 1c). Precipitation must occur once the polymer chains exceed the critical entanglement molecular weight to ensure polymer film integrity and high spatial resolution. Therefore, fine control of the polymer-solvent interaction is critical in IPP, as both low solubility and high final molecular weight are necessary conditions for the formation of a stable (swollen) polymer film.

Polyacrylonitrile (PAN), obtained by the free-radical addition reaction of its monomer, acrylonitrile (AN), satisfies all these requirements. While AN has some solubility in water, PAN is insoluble in both AN and water. We therefore chose to demonstrate IPP printing with the free-radical chain-growth reaction of AN with a water-soluble photoinitiator (Figure

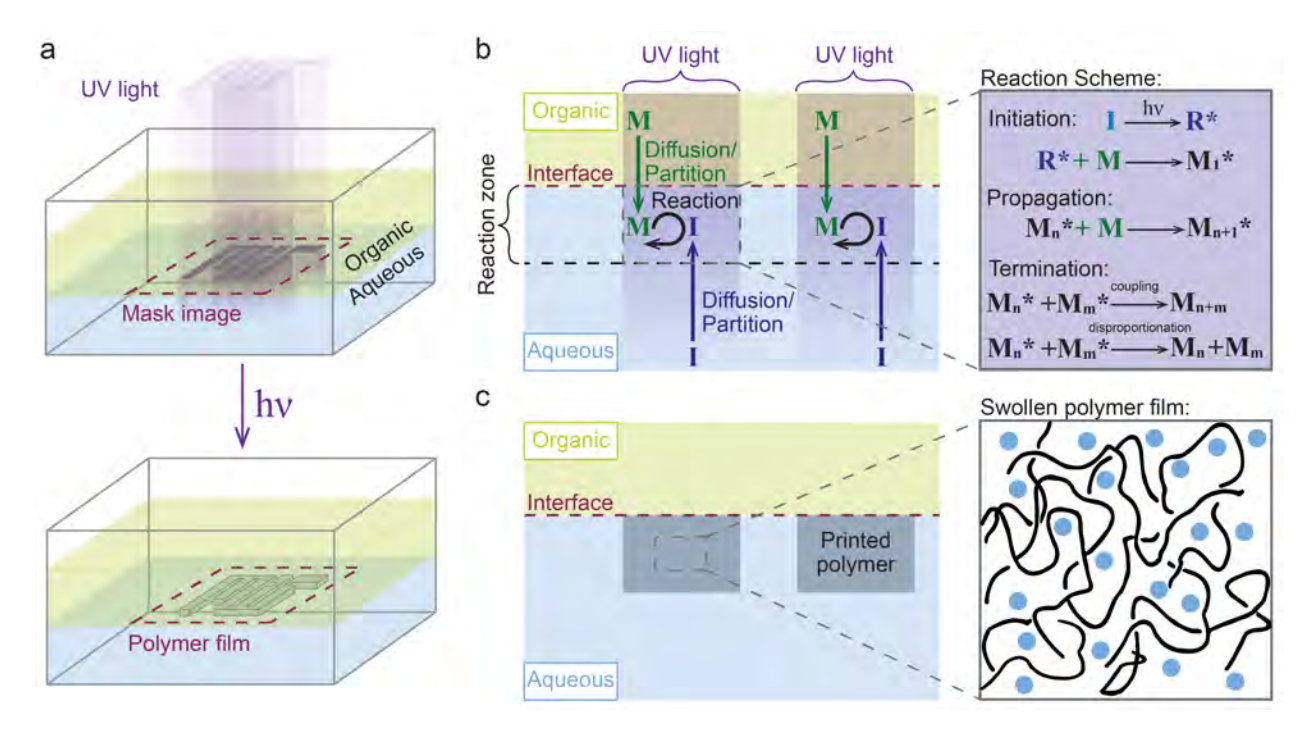


Figure 1: Overview of the IPP printing process. (a) Two immiscible liquids, each containing one of the reactants, form an interface. A UV image of a photomask is projected at the interface and triggers free-radical polyaddition and polymer film formation in the exposed areas. (b) The aqueous photoinitiator (I) dissociates to its radical form $(R\star)$, which reacts at the liquid-liquid interface with a monomer molecule (M) from the organic phase to create an active radical $(M\star)$, that in turn propagates to form a polymer chain. (c) Immiscible polymer chains precipitate out of solution and form a solid, swollen polymer layer in the exposed regions of the interface.

2). The organic phase was chosen to be pure (inhibitor-free) AN. We hypothesized that the polymerization reaction would occur on the aqueous side of the interface upon UV exposure, due to the greater solubility of AN in water than of the initiator in the organic phase (Figure 2a). The aqueous phase comprised a water-soluble photoinitiator dissolved in a 37.5 vol.% glycerol-water solution. The addition of glycerol increased the density of the aqueous phase, thereby preventing the PAN film from sinking over extended periods of times (~minutes). We experimented with two commercially-available water-soluble azo-photoinitiators (V-50 and VA-044; Wako Chemicals, Richmond); each with an absorption maximum at 365 nm, a convenient UV-A wavelength accessible with numerous LED systems (Figure 2b). Both initiators are expected to result in cationic end-groups with different reactivity and overall

stability. Due to its non-nitrile nature, VA-044 is usually less active than V-50 at room temperature but also less prone to hydrolysis, resulting in a stable non-radical decomposition product.²⁹

Demonstration of IPP and in-plane resolution assessment

To demonstrate and study IPP, we designed and built a single-layer projection-based printing system with a bottom-view camera to assess in-plane resolution (Figure 2c). A custom-made quartz photomask was illuminated by the diffused light from a UV LED. The mask image was then collimated and refocused at the liquid-liquid interface using an afocal optical train. Using this setup, we successfully printed PAN films at the AN-aqueous interface (Figure 2d-e). As expected, the PAN film formed on the aqueous side of the interface. The chemical structure of PAN obtained by IPP printing was confirmed and compared to commercially-available PAN using nuclear magnetic resonance (NMR), fourier-transform infrared (FT-IR) spectroscopy and thermogravimetric analysis (TGA). More information about the polymer structure confirmation can be found in the Supporting Information (SI).

The in-plane resolution of the IPP printing process was assessed using a modified version of the USAF 1951 resolution target,³⁰ and experiments were performed with a range of concentrations of each photoinitiator type (Figure 3). A quartz mask was fabricated with a modified pattern consisting of connected feature groups, in order to avoid erroneous measurement due to the free motion of the printed objects at the liquid-liquid interface (Figure 3a). The image of the target was projected at the liquid-liquid interface and the spatial fidelity of the PAN film in different printing conditions was assessed by extracting the intensity profile across the pattern (Figure 3b). The limit of resolution was extracted from the largest element observed where the three constitutive lines could no longer be distinguished spatially from each other (Figure 3c,d). In PAN films obtained from V-50 and VA-044, this occurred in one of Group 3 or 4 subgroups, depending on photoinitiator type and concentration.

The value of resolution was therefore evaluated as the width of a single line from the first

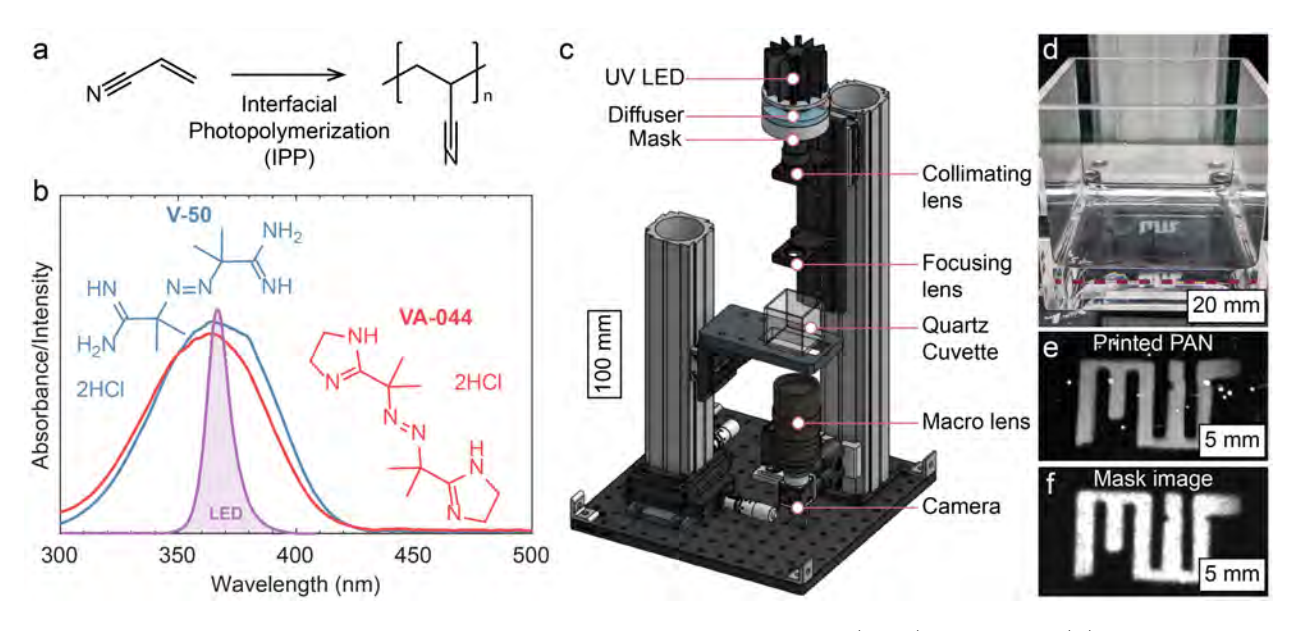


Figure 2: Demonstration of interfacial photopolymerization (IPP) of PAN. (a) Free radical polymerization reaction of PAN from AN partitioned into the aqueous phase. (b) Absorbance spectra of the selected aqueous photoinitiators, and comparison with the emission spectrum of the 365-nm LED light source. (c) 3D rendering of the single-layer IPP printing apparatus. (d) Photograph of quartz cuvette containing the reaction medium, and the letters MIT after exposure of the liquid-liquid interface. Close-up view of (e) the printed MIT pattern and (f) the photomask geometry.

non-resolved subgroup in the printed PAN image (Figure 3e). ³⁰ We find that, at low initiator concentration $[I]_0$, the smallest linewidth decreased with increasing initiator concentration until reaching a minimum. Further increase of the initiator concentration beyond the point of highest resolution resulted in a larger linewidth which, in the case of V-50, reached a plateau value at $[I]_0 = 1.0$ wt.%. This evolution with initiator concentration is consistent with the internal filter effect of photopolymerization reactions: ^{31–33} a very high photoinitiator concentration induces absorption of the incident UV light over a smaller volume, resulting in a slowdown of the polymerization reaction ³⁴ and a decrease of the final polymer molecular weight. ³⁵ This becomes more significant for photoinitiators with a high molar absorption coefficient ³³ and a high photodecomposition rate k_d , ³² explaining why V-50 ($k_d = 4.82 \cdot 10^{-5}$ s⁻¹) appears to feature a sharper maximum than its less reactive VA-044 counterpart ($k_d = 7.5 \cdot 10^{-6}$ s⁻¹). ²⁹ In the studied UV exposure conditions (30 s at 468 W m⁻²), the smallest linewidth was 40 μ m in the case of V-50 ($[I]_0 = 0.6$ wt.%), and 55 μ m in the case of VA-044

($[I]_0 = 1.0 \text{ wt.\%}$). These values are comparable to other projection-based vat-polymerization printing methods such as Digital Light Processing (DLP) printing. ^{36,37}

We also observed the formation of gas bubbles trapped at the liquid-liquid interface upon UV exposure, due to the generation of nitrogen as a by-product of the azo initiator decomposition reaction. ²⁹ More details about nitrogen generation during photoinitiation can be found in SI. The amount of nitrogen generated and its dependence on initiator concentration can also contribute to decreased resolution and is quantified by the number of bubble observed within the field of view of the camera (Figure 3f). We found that the number of bubbles detected increased with $[I]_0$, due to the higher rate of photodecomposition. Here again, the bubble count increased more slowly in the case of VA-044 than for V-50 due to the slower dissociation rate constant of VA-044. ²⁹

Measurement and modeling of film growth kinetics in IPP

Next, in order to evaluate the potential of IPP for photoprinting thin films and threedimensional objects, we characterized the evolution of polymer layer thickness δ as a function of printing parameters. We found that the PAN layer thickness increases linearly with exposure time, while number-average (M_n) and weight-average (M_w) molecular weights remain constant. Photoinitiator type did not affect δ , but VA-044 resulted in lower M_n and M_w values than V-50 (Figure 4a,b). This is consistent with the lower in-plane resolution achievable with VA-044 as shorter polymer chains give lower entanglement.

To develop a more quantitative, predictive understanding of the influence of processing parameters on print speed and polymer properties, we derived a macrokinetics model of IPP and calibrated the rate constants of propagation and termination to match the evolution of film thickness with exposure time observed experimentally (Figure 4c). As supported by experimental observation, we consider that the IPP reaction occurs in a shallow volume on the aqueous side of the interface (Figure 4c). The depth of the reaction zone ϵ corresponds to the depth to which the photoinitiator can effectively absorb the excitation light in the

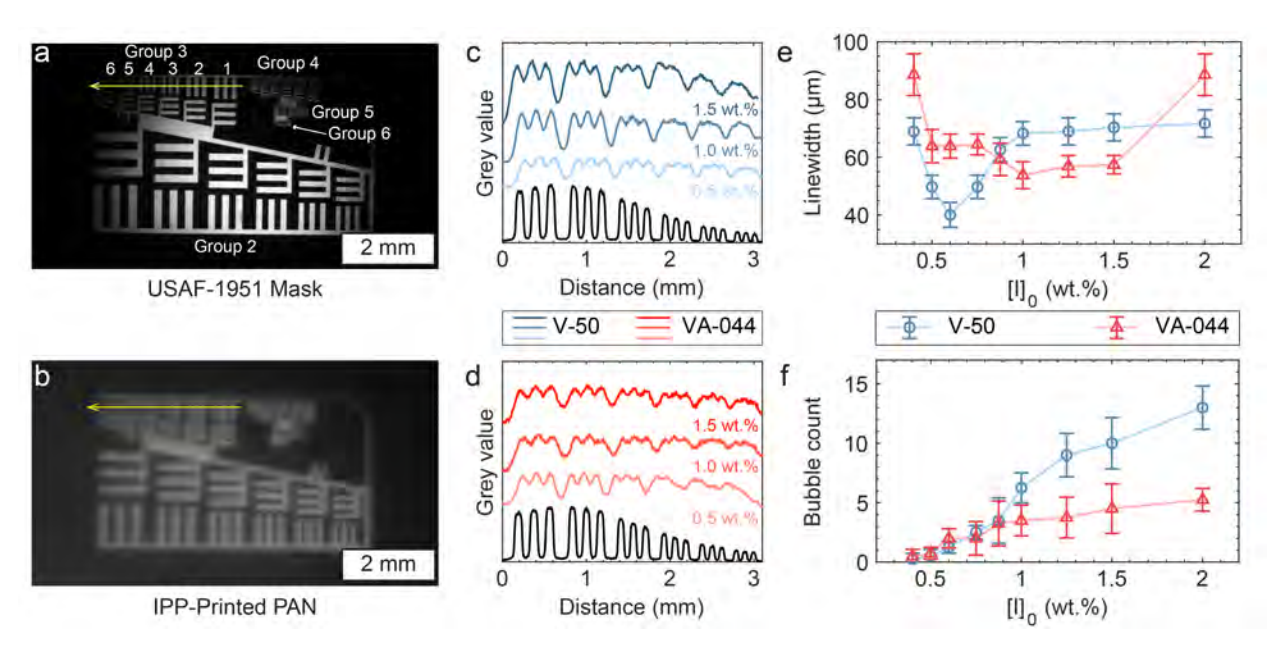


Figure 3: In-plane resolution assessment for IPP of PAN. (a) Projection of the custom USAF-1951 photomask focused at the liquid-liquid interface. (b) PAN film image of target obtained from IPP using 0.6 wt.% V-50. The yellow arrow indicates the line and direction of the intensity profile represented in (c,d). (c-d) Intensity profiles for Group 3 at 0.5, 1.0, and 1.5 wt.% of (c) V-50 and (d) VA-044. The resolution limit corresponds to the first group where the lines can no longer be resolved from the intensity profile, and the black line represents the intensity profile obtained in the image plane of the photomask. (e) Limit of resolution defined as the single linewidth in the identified group and (f) gas bubble count in each image of printed PAN films versus photoinitiator concentration and type. Markers and error bars represent the average and standard deviation over five PAN films obtained in the same conditions. All prints were obtained using a 30s exposure time.

aqueous phase, as diffusion/partition of AN into the aqueous phase is found to be relatively fast due to the affinity of the monomer for water. All concentration profiles are linearized in the space of the phases to obtain a system of coupled ordinary differential equations with time. This first-principles model takes into account reactive species transport, polymerization reaction kinetics, and precipitation of polymer chains to predict the time-dependent evolution of relevant species concentration and polymer film properties. Combining the theoretical frameworks used for bulk photopolymerization and interfacial polycondensation, we derived a set of governing equations for the concentration of relevant chemical species in the reaction zone. The concentration of initiator in the reaction zone $[I]_r$ is governed by:

$$\frac{d[I]_r}{dt} = +\frac{k_{L,I}}{\epsilon} \left([I]_a - [I]_r \right) - 2\phi \mathcal{I}_{abs} \tag{1}$$

where $k_{L,[I]}$ is the mass transfer coefficient for the initiator between the bulk aqueous phase and the reaction zone, ϵ is the depth of the reaction zone, $[I]_a$ is the initiator concentration in the bulk of the aqueous phase, ϕ is the quantum yield of the photoinitiator, and \mathcal{I}_{abs} is the volumetric intensity of the absorbed light.

We assume steady state, i.e. that the radicals produced by photoinitiation immediately initiate polymerization. From there, the governing equations in the reaction zone for activated monomer $[M*]_r$ and polymer chains (number of repeat units n > 1) $[M_n*]_r$ follow:

$$\frac{d[M*]_r}{dt} = -k_p [M*]_r [M]_r + 2\phi \mathcal{I}_{abs} - k_{tc} [M*]_r \sum_{k=2}^{\infty} [M_k*]_r$$
 (2)

$$\frac{d [M_n *]_r}{dt} = k_p [M *]_r ([M_{n-1} *]_r - [M_n *]_r) - k_{tc} [M_n *]_r \sum_{k=2}^{\infty} [M_k *]_r$$
(3)

where k_p and k_{tc} are the rate constants of propagation and termination, respectively. The subscript

Finally, the concentrations of terminated polymer chains in the reaction zone $[M_2]_r$ (n > 1) are obtained following:

$$\frac{d\left[M_2\right]_r}{dt} = k_{tc} \left[M*\right]_r \left[M*\right]_r \tag{4}$$

$$\frac{d [M_n]_r}{dt} = k_{tc} \sum_{k=1}^{\left[\frac{n-1}{2}\right]} [M_{n-k} *] [M_k *]$$
(5)

We also consider that instant precipitation occurs when the volume fraction φ_n of polymer chains of size n becomes equal to the solution of the spinodal envelope given by:

$$\varphi_n^2 + \left(\frac{m_n - 1}{2m_n \chi} - 1\right) \varphi_n + \frac{1}{2m_n \chi} = 0 \tag{6}$$

where χ is the PAN-water interaction parameter, and φ_n is the volume fraction of chains of size n in the reaction zone. More information on the derivation and choice of numerical values for the model can be found in SI.

The rates of propagation and termination in free-radical polymerization depend greatly on the reaction conditions such as solvent choice or photoinitiator type. This is particularly the case for the free-radical polymerization of AN in an aqueous medium. 38 We therefore calibrated the rate constants of propagation (k_p) and termination (k_{tc}) to match the experimentally observed temporal evolution of PAN film thickness and molecular weight (Figure 4b,c). All films were printed using the optimal photoinitiator concentration obtained from in-plane resolution measurements (0.6 wt.% for V-50 and 1.0 wt.% for VA-044) and the reaction zone depth was assumed to be the height of aqueous phase (2 mm). We calibrated the propagation rate constant $k_p = 3.5 \text{ m}^3 \text{ mol}^{-1} \text{ s}^{-1}$ for both photoinitiators, as chain propagation is considered independent of initiator type. This value is in agreement with reported values for the aqueous polymerization of acrylonitrile. ³⁸ For V-50, we fixed the termination rate constant $k_{tc} = 1 \cdot 10^3 \text{ m}^3 \text{ mol}^{-1} \text{ s}^{-1}$, and quantum yield $\phi = 0.38.39$ Model calibration for VA-044 resulted in a greater value of $k_{tc} = 8 \cdot 10^3 \text{ m}^3 \text{ mol}^{-1} \text{ s}^{-1}$ and a smaller value of $\phi = 0.23$. The lower quantum yield value is consistent with the lower photodecomposition rate of VA-044 compared to V-50. The greater termination constant in the case of VA-044 and lower polymer molecular weight can be explained by potential chain transfer with the initiator, steric effects, or the influence of different end groups on PAN solubility. The values of k_{tc} found here are consistent with reported values for free-radical polymerization of AN in water. 38 The termination rate constant is found to be lower than for typical free-radical polymerization reactions due to precipitation of PAN and trapping of the radicals within solid particles. 38,40 Values for the remaining model parameters and initial conditions were fixed at values either measured experimentally or obtained from the literature (Table S2).

With the above calibration, the evolution of δ and polymer molecular weight with exposure time was successfully predicted by the model (Figure 4a-b). However, the polydispersity index (PDI) observed experimentally was greater than that calculated by the model. We measured PDIs of 2.1 and 2.3 for V-50 and and VA-044, respectively, compared to the calculated values of 1.2 and 1.3. This difference can be explained by the simplifying assumptions used to derive the model. The presence of light scattering on the precipitated polymer film and potential chain transfer reactions are expected to broaden the molecular weight distribution, explaining the greater experimental PDI values.

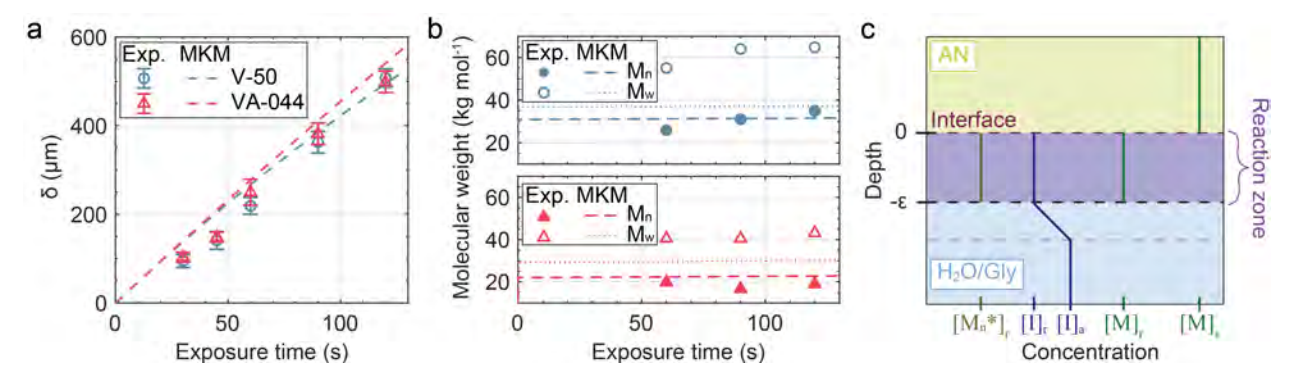


Figure 4: Experimental measurement (Exp.) and macrokinetics modeling (MKM) of film growth kinetics in IPP. (a,b) Evolution of (a) the thickness δ and of (b) the number-average (M_n) and weight-average (M_w) molecular weights of the printed PAN film with exposure time. These experimental measurements were used to calibrate a macrokinetics model (MKM) described schematically in (c). Concentrations profiles near the liquid-liquid interface for monomer, initiator and propagating radicals are plotted in the space of the phase and considered constant in space in the reaction zone. Calibration of the polymerization propagation and termination constants was performed against experimental data obtained at the optimal photoinitiator concentrations for minimum linewidth printing (0.6 wt.% V-50 and 1.0 wt.% VA-044) and for a reaction zone of depth $\epsilon = 2$ mm (height of the aqueous phase).

Using the macrokinetics model calibrated to the V-50 photoinitator, we performed a parametric analysis of the relationships among key process parameters, shown in Figure 5. First, we predict the influence of $[I]_0$ on IPP kinetics, and therefore print speed defined by the polymer film thickness. Increasing initiator concentration results in a faster-growing PAN film (Figure 5a,b) yet a lower molecular weight polymer (Figure 5c). While we did not observe PAN film formation at 0.25 wt.% photoinitiator, the model predicted the formation of a 5 μ m

film after 60 s of exposure (Figure 5a). This difference resides in the simplifying assumption of the model that at t = 0, all polymer chain concentrations are at their saturation limit in the aqueous solution, which is not necessarily the case experimentally. On this point, prior to each PAN printing experiment, the liquid-liquid interface was exposed for 5-10 minutes to the same light intensity used for printing (468 W m⁻²) to increase the concentration of PAN in the aqueous phase to be close to its saturation limit. This enables precipitation to occur at the start of the printing process. As a result, subsequent exposures caused film precipitation in timescales in the order of seconds, while the model predicts instantaneous polymer film formation.

The model predicts a linear relationship between initiator concentration and PAN film thickness obtained after a fixed exposure time, indicating a pseudo-first order reaction in initiator concentration (Figure 5b). This linear dependence is commonly observed in interfacial polycondensation of low-reactivity monomers, such as diol-carboxylic acid systems, ^{24,41} or diamine-dinanhydride pairs. ⁴² In the case of slow interfacial polymerization kinetics, the reaction takes place in a homogeneous manner (on a microscopic scale) in a zone of finite thickness. ⁴¹ While the polymerization reaction mechanism is different in the case of free-radical IPP of PAN, we expect to see the same linear dependence due to the relatively low value of the polymerization rate constants.

The model also explains that both M_n and M_w decrease with increasing $[I]_0$, while the PDI increases (Figure 5c). This is consistent with classic free-radical polymerization kinetic theory and is further exacerbated by the trapped radical effect reflected in the low calibrated value of k_{tc} . Note that the model does not take into account the internal filter effect or light scattering observed experimentally, which are expected to reduce film growth rate and affect both molecular weight and PDI at high initiator concentrations.

The model was also used to predict the influence of the reaction zone depth ϵ on film formation by IPP (Figure 5d-f). Practically, the reaction zone depth can be adjusted by tailoring the light penetration depth.⁴³ We found that print speed increased with ϵ (Figure

5d) and that controlling the reaction zone depth can promote fine control of the vertical resolution, defined as the relationship between thickness and time (Figure 5e). Here again, $\delta(30s)$ increases linearly with ϵ . The faster print speed with increasing reaction zone depth is the result of the low molar absorption coefficient of the azo initiators used in this work (21 L mol⁻¹ cm⁻¹) compared to other conventional photoinitiators with similar absorption wavelengths (100 – 1000 L mol⁻¹ cm⁻¹). ⁴⁴ As the light absorption in the aqueous phase is low, increasing the depth over which the reaction can occur results in a higher number of activated initiator molecules and therefore a greater reaction yield. Molecular weight and PDI are predicted to be independent of the reaction zone depth (Figure 5f).

These predictions provide insight on how IPP parameters can be adjusted to tailor the final polymer properties. Controlling ϵ enables tuning of print speed without affecting final molecular weight. Yet, adjustment of the initiator concentration $[I]_0$ influences significantly both final film thickness and polymer molecular weight distribution.

Multilayer IPP printing

Last, IPP printing was performed in a multilayerscheme to demonstrate possible translation from thin film formation to 3D printing. To do this, we designed and assembled a build plate attached to a vertical translation stage and used the best film printing conditions for V-50 explained above. Before illumination, the build plate was brought within 100 μ m below the liquid-liquid interface (Figure 6a). UV illumination was then turned on to induce polymerization, precipitation, and formation of the first polymer layer. For subsequent layers, the build plate was lowered by 100 μ m from its previous position, and exposure was resumed for 30 s. We found that the print height h_p increased linearly with the number of layers n_{layer} , as it is to be expected for a vat polymerization 3D printing process (Figure 6b). Yet, a linear fit of the evolution of h_p with n_{layer} indicated that the thickness increased only 50 μ m with each subsequent exposure.

We used the same (fixed) mask geometry to print up to 7 consecutive layers (Figure

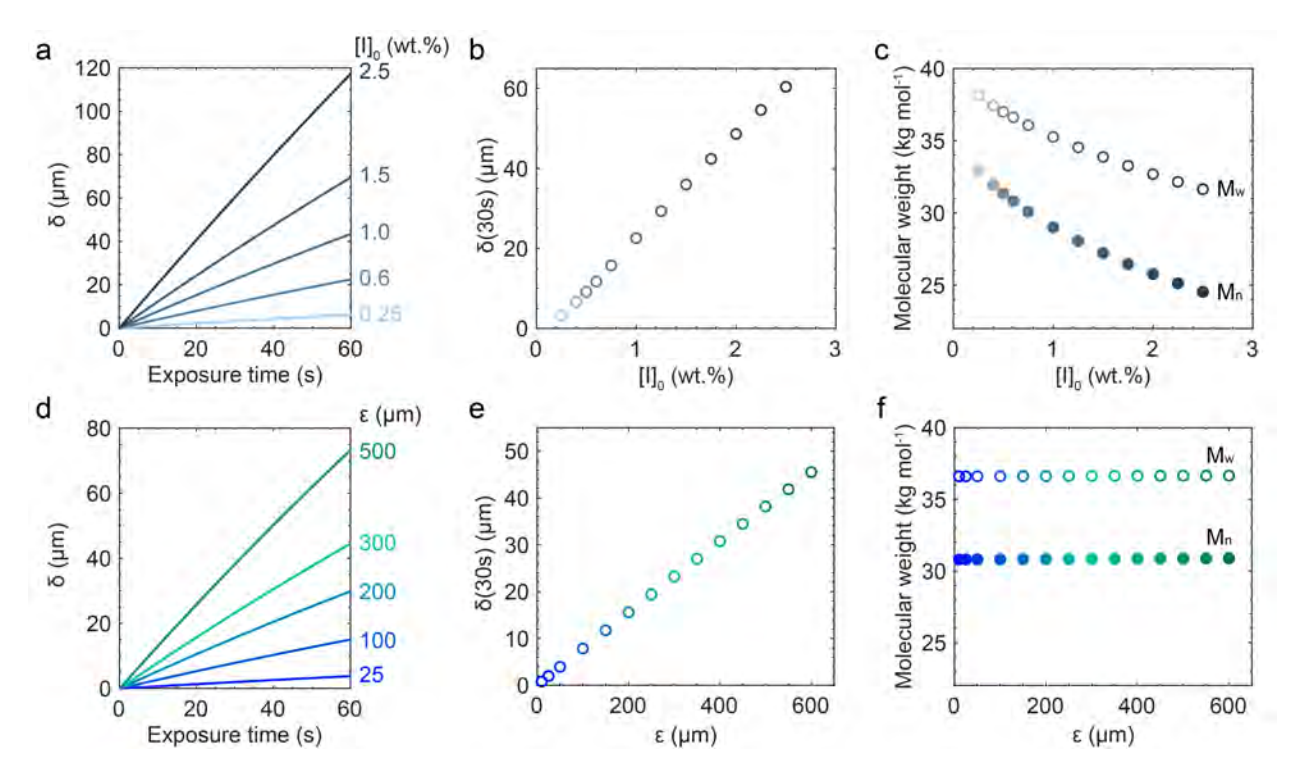


Figure 5: PAN film thickness and molecular weight prediction using the macrokinetic model with rate constants calibrated for the V-50 initiator. (a) Film thickness evolution with exposure time for selected initiator concentrations in the aqueous phase. Relationships between (b) calculated film thickness and (c) molecular weight evolution with initiator concentration. Exposure time was fixed at 30 s and $\epsilon = 150~\mu\text{m}$. (d) Relationship between PAN film thickness and exposure time for different values of the reaction zone depth. Relationships between (e) film thickness and (f) molecular weight versus reaction zone depth, at fixed exposure of 30 s and initial condition for initiator concentration $[I]_a(0) = [I]_r(0) = 0.6~\text{wt.}\%$).

6c-e). The prints had good spatial fidelity; however, we note the presence of cracks and bubbles, likely due to nitrogen generation upon photoinitiator dissociation. Additionally, the presence of polymer outside of the exposed area became more prominent in thicker prints, likely due to light scattering on the previous printed PAN layers and unwanted activation of the photoinitiator outside of the exposed regions.

Scanning Electron Microscopy (SEM) cross sections showed layering of the printed PAN, with alternation of high-density layers containing little residual glycerol, and low-density polymer layers with large amounts of glycerol swelling the polymer (Figure 6f). Cracks were found in the weaker highly swellen regions while avoiding the higher-density PAN layers (Figure 6g). This layered structure can be explained by two main causes. First, the z-step was

 $100 \,\mu\text{m}$, while the measured layer height was found to be $50 \,\mu\text{m}$, indicating that solid polymer did not form in the entire volume of the reaction zone. This also matches the prediction of the macrokinetics model where the polymer film is always found to be thinner than the defined reaction zone after 30 s exposure. Second, in conventional interfacial polycondensation, the density of polymer films decreases through their thickness, due to polymer precipitation at the liquid-liquid interface that hinders diffusion of the monomer into the reaction zone away from the interface. While the polymerization reaction mechanism is different here, IPP remains diffusion limited, similarly to conventional interfacial polycondensation. It is therefore unsurprising to see a decrease in polymer density with increasing PAN layer thickness, particularly in combination with decreasing photoinitiator activation caused by light scattering from the precipitated polymer.

Discussion

Bringing together the demonstration of single-layer and multilayer printing of PAN with the macrokinetics model predictions, we showed that IPP can achieve sub-100 μ m resolution, which is comparable to projection-based vat-polymerization printing of thermosets,. ^{36,37} Inplane resolution, film thickness, and interlayer adhesion are all greatly influenced by reaction kinetics and final polymer molecular weight. Increasing $[I]_0$ in IPP results in faster printing due to a higher rate for the initiator and propagation reactions. However, internal filter effects and change in the rate of initiation result in a drop of molecular weight at high initiator concentration. This decrease in chain length affects resolution drastically by reducing interchain interaction and overall entanglement. Reducing the depth of the reaction zone ϵ enables adjustment of the print without affecting polymer entanglement. Tailored ϵ values can be obtained by fine adjustment of the position of the light-absorbing build plate, or increasing light absorption in the reaction phase through addition of a non-reactive dye. The addition of a light-absorbing species is also anticipated to reduce light scattering and increase printing resolution further. However, adjustment of the reaction zone depth adjustment still

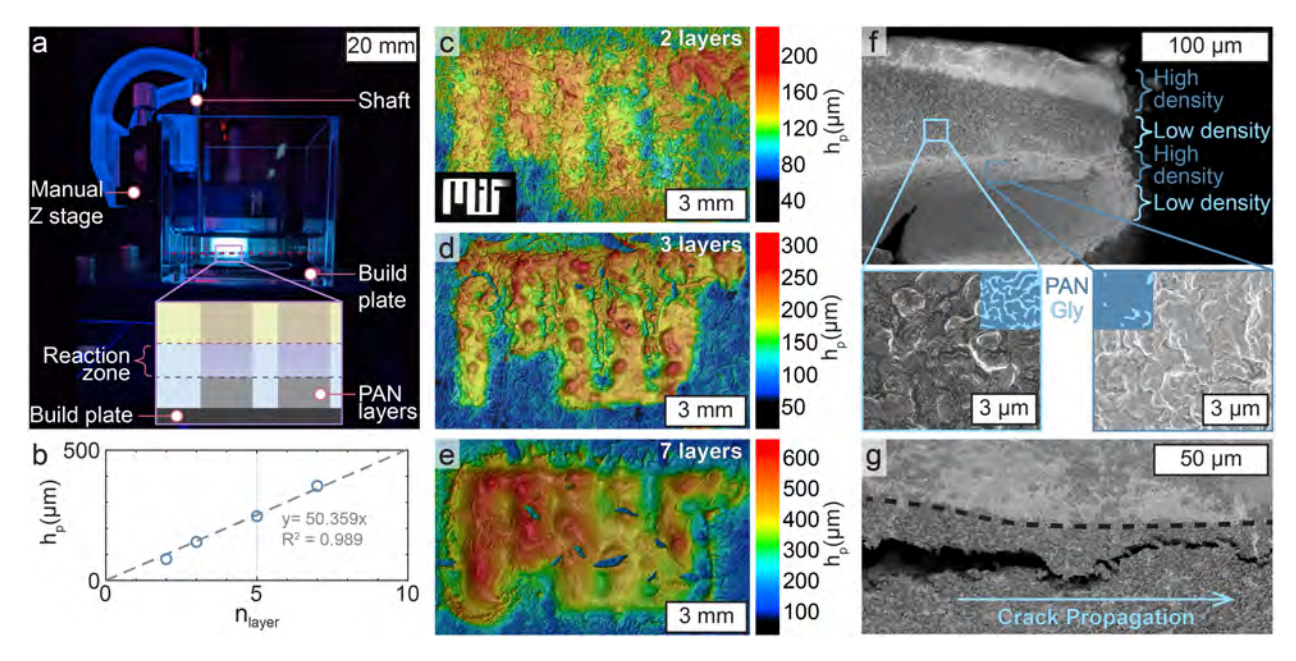


Figure 6: IPP multilayer printing. (a) Photograph of the manual build plate apparatus and schematic showing its position compared to the liquid-liquid interface. (b) Linear dependence of the height (h_p) of the print on the number of printed layers. (c-e) Height profiles of the letters M.I.T printed using IPP of (c) two, (d) three, and (e) seven layers. Inset shows the photomask image in absence of polymerization. (f) SEM cross-section of a PAN object printed with IPP, showing layering of the printed polymer, with alternation of high-density and low density layers of PAN swollen with glycerol. (g) SEM view of a crack propagating within the lower-density, highly swollen regions while avoiding the higher-density PAN layer. All prints were obtained for 0.6 wt.% V-50, a single layer exposure time of 30 s, and an vertical z-step of 100 μ m.

results in a trade-off between resolution and print speed, as a shallower reaction zone results in a thinner yet slower-growing PAN film. This is particularly problematic in implementing IPP in 3D printing scheme, where at short exposure time, the thickness of the polymer film formed is almost always smaller than the reaction zone depth, exacerbating density gradients and porosity in the final part.

While the challenges discussed here are important to overcome for further development of IPP as 3D printing method, process optimization follows a similar path as that for established vat photopolymerization techniques. ⁴⁵ Moreover, while IPP was demonstrated on PAN, its implementation can be expanded to other polymer systems. Most linear-chain polymers are soluble in their monomer, due to similarities in chemical structure. ⁴⁶ This makes their

implementation in IPP inherently challenging. However, this can be overcome by adding to the organic phase a solvent that is both miscible with the monomer and an anti-solvent for the polymer. Ongoing work extends IPP to other polymers and seeks to improve the characteristics of multilayer artifacts.

Conclusion

We introduced interfacial photopolymerization (IPP), a method for photoprinting of linear chain polymers relying on photoinitiated interfacial polyaddition of a free-radical monomer. We successfully identified the process requirements and demonstrated IPP both in single layer and multilayer vat polymerization printing of PAN. We showed that the resolution of IPP can be comparable to that of other projection-based UV printing methods and experimentally studied how initiator type and concentration affect spatial fidelity and final polymer properties. A first-principle macrokinetics model enabled prediction of PAN film properties with process parameters. We found experimental and theoretical evidence of a trade-off between print speed and spatial resolution as commonly observed for other photoprinting processes. While IPP was used as the first demonstration of photoprinting of PAN, we expect that it can be expanded to other commodity thermoplastics in future work.

Acknowledgement

Financial support was provided by the National Science Foundation (CMMI-2114343) and by a gift from the Ryder Charitable Foundation. C.A.C. was supported by a MathWorks Engineering Fellowship at MIT for academic years 2020-2021 and 2021-2022. The authors thank: Prajwal Tumkur Mahesh, Jada Jackman, and Alison Grafton for their support in conducting multilayer printing experiments and verifying repeatability of the IPP process; Ryan Oliver, Benjamin Miller and Mathias Kolle for their input in the design and assembly of the projection optical train; Daniel Gilbert, Paul Carson, and Joseph D. Sandt for

help with design and manufacturing of custom mechanical parts for the printing setup; Carl Thrasher for support with gel permeation chromatography measurements and valuable feedback on the manuscript; and Prof. Zachary P. Smith and Dr. Justin Teesdale for access to thermogravimetric analysis tools and associated support. This work made use of the electron microscopy facilities at MIT.nano, and nuclear magnetic resonance instruments in the Department of Chemistry Instrumentation Facility (DCIF) at MIT.

Supporting Information Available

Experimental procedures, Nitrogen generation in IPP, Structure and properties of IPP PAN, Macrokinetics model

References

- (1) Chowdhury, M. R.; Steffes, J.; Huey, B. D.; McCutcheon, J. R. 3D printed polyamide membranes for desalination. *Science* **2018**, *361*, 682–686.
- (2) Seisyan, R. P. Nanolithography in microelectronics: A review. *Technical Physics* **2011**, 56, 1061.
- (3) Camposeo, A.; Persano, L.; Farsari, M.; Pisignano, D. Additive Manufacturing: Applications and Directions in Photonics and Optoelectronics. Advanced Optical Materials 2019, 7, 1800419.
- (4) Gates, B. D.; Xu, Q.; Stewart, M.; Ryan, D.; Willson, C. G.; Whitesides, G. M. New Approaches to Nanofabrication: Molding, Printing, and Other Techniques. *Chemical Reviews* 2005, 105, 1171–1196, PMID: 15826012.
- (5) Sirbubalo, M.; Tucak, A.; Muhamedagić, K.; Rahić, O.; Čekić, A.; Vranić, E.

- Photopolymerization-Based Technologies for Microneedle Arrays Production. CMBE-BIH 2021. Cham, 2021; pp 670–678.
- (6) Skoog, S. A.; Goering, P. L.; Narayan, R. J. Stereolithography in tissue engineering.

 Journal of Materials Science: Materials in Medicine 2014, 25, 845–856.
- (7) Chiulan, I.; Heggset, E. B.; Voicu, S. I.; Chinga-Carrasco, G. Photopolymerization of Bio-Based Polymers in a Biomedical Engineering Perspective. *Biomacromolecules* 2021, 22, 1795–1814, PMID: 33819022.
- (8) Song, Y.; Gui, C.; Huo, Z.; Lee, S. W. R.; Liu, S. Mechanical system and dynamic control in photolithography for nanoscale fabrication: A critical review. *International Journal of Mechanical System Dynamics* **2021**, *1*, 35–51.
- (9) Magazine, R.; van Bochove, B.; Borandeh, S.; Seppälä, J. 3D inkjet-printing of photocrosslinkable resins for microlens fabrication. *Additive Manufacturing* **2022**, *50*, 102534.
- (10) Evans, S. E.; Harrington, T.; Rodriguez Rivero, M. C.; Rognin, E.; Tuladhar, T.; Daly, R. 2D and 3D inkjet printing of biopharmaceuticals – A review of trends and future perspectives in research and manufacturing. *International Journal of Pharma*ceutics 2021, 599, 120443.
- (11) Layani, M.; Wang, X.; Magdassi, S. Novel Materials for 3D Printing by Photopolymerization. *Advanced Materials* **2018**, *30*, 1706344.
- (12) Al Rashid, A.; Ahmed, W.; Khalid, M. Y.; Koç, M. Vat photopolymerization of polymers and polymer composites: Processes and applications. Additive Manufacturing 2021, 47, 102279.
- (13) Sampson, K. L.; Deore, B.; Go, A.; Nayak, M. A.; Orth, A.; Gallerneault, M.; Malenfant, P. R. L.; Paquet, C. Multimaterial Vat Polymerization Additive Manufacturing. ACS Applied Polymer Materials 2021, 3, 4304–4324.

- (14) van Bochove, B.; Grijpma, D. W. Photo-crosslinked synthetic biodegradable polymer networks for biomedical applications. *Journal of Biomaterials Science*, *Polymer Edition* 2019, 30, 77–106, PMID: 30497347.
- (15) Gojzewski, H.; Guo, Z.; Grzelachowska, W.; Ridwan, M. G.; Hempenius, M. A.; Grijpma, D. W.; Vancso, G. J. Layer-by-Layer Printing of Photopolymers in 3D: How Weak is the Interface? ACS Applied Materials & Interfaces 2020, 12, 8908–8914, PMID: 31961120.
- (16) Voet, V. S. D.; Guit, J.; Loos, K. Sustainable Photopolymers in 3D Printing: A Review on Biobased, Biodegradable, and Recyclable Alternatives. *Macromolecular Rapid Communications* 2021, 42, 2000475.
- (17) Kloxin, C. J.; Bowman, C. N. Covalent adaptable networks: smart, reconfigurable and responsive network systems. *Chem. Soc. Rev.* **2013**, *42*, 7161–7173.
- (18) Bao, Y.; Paunović, N.; Leroux, J.-C. Challenges and Opportunities in 3D Printing of Biodegradable Medical Devices by Emerging Photopolymerization Techniques. *Advanced Functional Materials* **2022**, *32*, 2109864.
- (19) Giboz, J.; Copponnex, T.; Mélé, P. Microinjection molding of thermoplastic polymers: a review. *Journal of Micromechanics and Microengineering* **2007**, *17*, R96–R109.
- (20) Martin, P. Thermoforming of polymers. Advances in Polymer Processing. Elsevier **2009**, 352–383.
- (21) Gao, X.; Qi, S.; Kuang, X.; Su, Y.; Li, J.; Wang, D. Fused filament fabrication of polymer materials: A review of interlayer bond. Additive Manufacturing 2021, 37, 101658.
- (22) Maghsoudi, K.; Jafari, R.; Momen, G.; Farzaneh, M. Micro-nanostructured polymer

- surfaces using injection molding: A review. *Materials Today Communications* **2017**, 13, 126–143.
- (23) Pantani, R.; Coccorullo, I.; Speranza, V.; Titomanlio, G. Modeling of morphology evolution in the injection molding process of thermoplastic polymers. *Progress in Polymer Science* **2005**, *30*, 1185–1222.
- (24) Morgan, P. W.; Kwolek, S. L. Interfacial polycondensation. II. Fundamentals of polymer formation at liquid interfaces. *Journal of Polymer Science Part A: Polymer Chemistry* 1996, 34, 531–559.
- (25) Sun, X.; Wang, X.; Sun, F.; Tian, M.; Qu, L.; Perry, P.; Owens, H.; Liu, X. Textile Waste Fiber Regeneration via a Green Chemistry Approach: A Molecular Strategy for Sustainable Fashion. *Advanced Materials* **2021**, *33*, 2105174.
- (26) Orabi, A. H.; Abdelhamid, A. E.-S.; Salem, H. M.; Ismaiel, D. A. New adsorptive composite membrane from recycled acrylic fibers and Sargassum dentifolium marine algae for uranium and thorium removal from liquid waste solution. *Journal of Radioanalytical and Nuclear Chemistry* 2020, 326, 1233–1247.
- (27) Yunessnia lehi, A.; Akbari, A. Novel membrane adsorbents prepared by waste fibers of mechanized carpet for Persian Orange X removal. *Environmental Nanotechnology, Monitoring & Management* **2017**, *8*, 209–218.
- (28) Bairagi, N. Recycling of textiles in India. J Textile Sci Engng 2014, 2, 003.
- (29) U. Rojas Wahl, R.; Zeng, L.; A. Madison, S.; L. DePinto, R.; J. Shay, B. Mechanistic studies on the decomposition of water soluble azo-radical-initiators. *J. Chem. Soc.*, *Perkin Trans.* 2 **1998**, 2009–2018.
- (30) Goncalves, D. P.; Griffith, D. J. Estimating uncertainty in resolution tests. *Optical Engineering* **2006**, *45*, 1 6.

- (31) Decker, C.; Moussa, K.; Bendaikha, T. Photodegradation of UV-cured coatings II. Polyurethane–acrylate networks. *Journal of Polymer Science Part A: Polymer Chemistry* 1991, 29, 739–747.
- (32) Zhang, S.; Li, B.; Tang, L.; Wang, X.; Liu, D.; Zhou, Q. Studies on the near infrared laser induced photopolymerization employing a cyanine dye-borate complex as the photoinitiator. *Polymer* **2001**, *42*, 7575–7582.
- (33) Kabatc, J.; Jedrzejewska, B.; Paczkowski, J. New heterobicationic hemicyanine dyes: Synthesis, spectroscopic properties, and photoinitiating ability. *Journal of Polymer Science Part A: Polymer Chemistry* **2006**, *44*, 6345–6359.
- (34) Jedrzejewska, B. Factors affecting the TMPTA radical polymerization photoinitiated by phenyltrialkylborates paired with tri-cationic hemicyanine dye. Kinetic studies. *Colloid and Polymer Science* **2013**, *291*, 2225–2236.
- (35) Zheng, H.; Liao, Y.; Zheng, M.; Zhu, C.; Ji, F.; Ma, J.; Fan, W. Photoinitiated Polymerization of Cationic Acrylamide in Aqueous Solution: Synthesis, Characterization, and Sludge Dewatering Performance. *The Scientific World Journal* **2014**, *2014*, 465151.
- (36) Ligon, S. C.; Liska, R.; Stampfl, J.; Gurr, M.; Mulhaupt, R. Polymers for 3D printing and customized additive manufacturing. *Chemical reviews* **2017**, *117*, 10212–10290.
- (37) Ghobadian, A.; Talavera, I.; Bhattacharya, A.; Kumar, V.; Garza-Reyes, J. A.; O'regan, N. Examining legitimatisation of additive manufacturing in the interplay between innovation, lean manufacturing and sustainability. *International Journal of Production Economics* 2020, 219, 457–468.
- (38) Eaton, R. S. The polymerisation of acrylonitrile in aqueous solution. Ph.D. thesis, University of Leeds, 1953.

- (39) Valdebenito, A.; Encinas, M. V. Effect of solvent on the free radical polymerization of N,N-dimethylacrylamide. *Polymer International* **2010**, *59*, 1246–1251.
- (40) Seymour, R. B.; Stahl, G. A. In *Recent Advances*; Carraher, C. E., Jr., J. P., Eds.; Interfacial Synthesis; Marcel Dekker, inc.: New York NY, 1982; Vol. 3; Chapter The reaction of vinyl monomers with "trapped free radicals", pp 135–139.
- (41) Johnson, E. D. A STUDY OF THE KINETICS AND MECHANISM OF INTERFA-CIAL POLYMERIZATION (NYLON 6,10, POLYAMIDE). Ph.D. thesis, 1985; Ph.D.
- (42) Chazot, C. A. C.; Thrasher, C. J.; Peraire-Bueno, A.; Durso, M. N.; Macfarlane, R. J.; Hart, A. J. Scalable, Versatile Synthesis of Ultrathin Polyetherimide Films and Coatings via Interfacial Polymerization. Advanced Functional Materials n/a, 2214566.
- (43) Dolinski, N. D.; Page, Z. A.; Callaway, E. B.; Eisenreich, F.; Garcia, R. V.; Chavez, R.; Bothman, D. P.; Hecht, S.; Zok, F. W.; Hawker, C. J. Solution Mask Liquid Lithography (SMaLL) for One-Step, Multimaterial 3D Printing. Advanced Materials 2018, 30, 1800364.
- (44) Neumann, M. G.; Miranda, W. G.; Schmitt, C. C.; Rueggeberg, F. A.; Correa, I. C. Molar extinction coefficients and the photon absorption efficiency of dental photoinitiators and light curing units. *Journal of Dentistry* **2005**, *33*, 525–532.
- (45) Tumbleston, J. R.; Shirvanyants, D.; Ermoshkin, N.; Janusziewicz, R.; Johnson, A. R.; Kelly, D.; Chen, K.; Pinschmidt, R.; Rolland, J. P.; Ermoshkin, A.; Samulski, E. T.; DeSimone, J. M. Continuous liquid interface production of 3D objects. *Science* 2015, 347, 1349–1352.
- (46) Hansen, C. M. Hansen solubility parameters: a user's handbook; CRC press, 2007.

TOC Graphic

